

Spatial Distribution of D-D/D-³He Advanced Fuels Fusion Reactions in an Inertial Electrostatic Confinement Device

K. Masuda 1), K. Yoshikawa 1), T. Ohishi 1), S. Ogawa 1), H. Zen 1), T. Takamatsu 1)
1) Inst. of Advanced Energy, Kyoto University, Kyoto, Japan

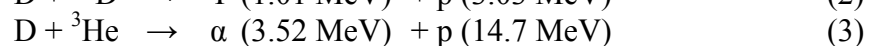
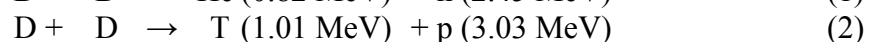
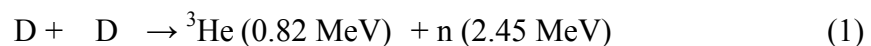
e-mail contact of main author: masuda@iae.kyoto-u.ac.jp

Abstract. An inertial electrostatic confinement (IEC) fusion device can produce copious amount of neutrons and protons from D-D and D-³He fusion reactions using D₂ and ³He fuels. In this study, the production rates of D-³He protons and D-D neutrons have been measured simultaneously as functions of operational parameters, namely D₂-³He fuel composition, the discharge bias voltage and the discharge current. As a result the optimal D₂-³He fuel composition is found for maximizing D-³He reactions. Also shown is a stronger dependence of D-³He reaction on the bias voltage than D-D, which is encouraging for a further enhanced D-³He rate with a higher bias voltage. Furthermore, we have revealed the spatial distribution of D-³He fusion reaction, and consequently the fractions of volumetric and embedded fusion contributions, both of which are essential for understanding the IEC mechanism and accordingly for innovative IEC-based concepts coming up such as the ion-source-assisted IEC, the multi-grid IEC and further innovative concepts. We found the volumetric contribution of ~40% concentrated within the cathode, which is very encouraging compared with an implication by previous experimental studies, i.e. a much larger contribution of the embedded D-³He fusion.

1. Introduction

An inertial electrostatic confinement (IEC) fusion device is a compact fusion-driven neutron/proton source with a simple configuration. It consists of a highly transparent gridded cathode concentrically held at the center of a spherical anode (see Figs. 1 and 2). Ions produced by a glow discharge between them are accelerated toward the center as they gain energy from the applied electric fields, and the spherical focusing of ions results in beam-beam and/or beam-gas colliding fusion reactions. An IEC device could be an ideal transportable neutron/proton source for versatile applications with its promising features; easy operation not requiring an expert operator, safety without radioactive isotope, high flux of neutrons and protons ($\sim 10^8 \text{ sec}^{-1}$ dc and $\sim 10^{10} \text{ sec}^{-1}$ pulse from D-D reactions) and their tenability. An important advantage over existing accelerator-driven beam-target-type fusion devices is that the use of ‘plasma target’ leads to capability of a long-pulse and even a dc operation, and a long lifetime without maintenance, with much reduced problems of heat-removal and sputtering from the target.

Equations (1) through (3) show the fusion reaction channels for D₂-³He fuels. Of particular interest, the protons from D-³He reactions are highly energetic enough to match the cross-sections for producing radioactive isotopes for medical use, e.g. Positron Emission Tomography (PET) [1], [2].



The promising advantage of the fusion-based proton source over proton accelerators is that the produced protons gain a huge energy from ‘fusion’, and therefore it needs only a moderate voltage ~ 100 kV for producing 14.7 MeV protons, leading to a potential application as an extremely compact source.

In IEC researches aiming at drastically enhanced neutron/proton yields required for further

extending their application, understanding the spatial distribution of fusion reactions is no doubt one of the most intensive interests. A localized volume of fusion reactions within the cathode is of course desirable and expected, while a more diverse distribution is also predicted resulting from the electric potential formation by the converging ions' and/or the ion-loss processes with the residual gas molecules. All of these are however still left unclear.

Furthermore, as of $D\text{-}^3\text{He}$ reactions, the proton yield can hardly be evaluated without obtaining the spatial distribution unlike $D\text{-}D$ reaction rates which can easily be measured by means of the neutron yield on assumption of a point source by use of a neutron counter set far away from the source outside vacuum. Also, early experimental results by $D_2\text{-}^3\text{He}$ fuel at University of Wisconsin, Madison [3] imply, unlike $D\text{-}D$, a strongly localized birthplace of $D\text{-}^3\text{He}$ protons on the cathode grids, i.e. fusion between deuterium beams and embedded ^3He is predominant, though the fractions of volumetric and embedded fusion contributions are left unclear. It should be noted that a large contribution from the embedded $D\text{-}^3\text{He}$ fusion is not desirable considering the aforementioned advantages over the beam-target type sources.

In this study, we assembled a proton counting system using a silicon diode detector and circular collimator masks of three different diameters on a linearly movable rod set between the detector and the IEC chamber, in order to make the aforementioned essential issues clear by determining the spatial distribution of $D\text{-}^3\text{He}$ reactions. Also, by use of a neutron counter together with the proton counting system, we measured $D\text{-}^3\text{He}$ and $D\text{-}D$ protons and neutrons simultaneously from an IEC device run by $D_2\text{-}^3\text{He}$ fuel gases. The production rates dependences were studied on the $D_2\text{-}^3\text{He}$ fuel composition, the discharge bias voltage applied to the inner transparent gridded cathode and the discharge current.

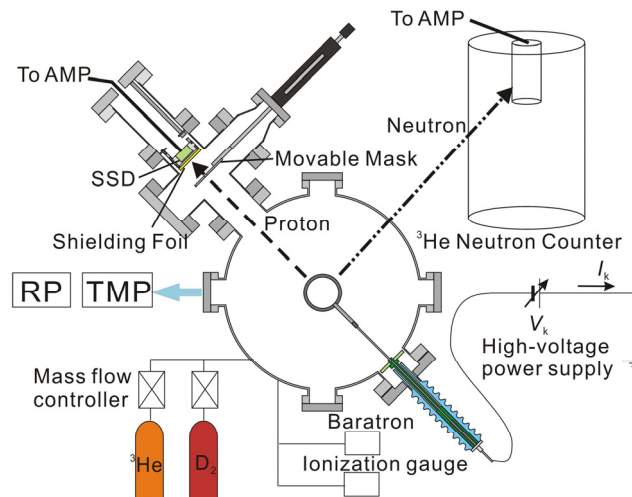


FIG. 1. Experimental setup.

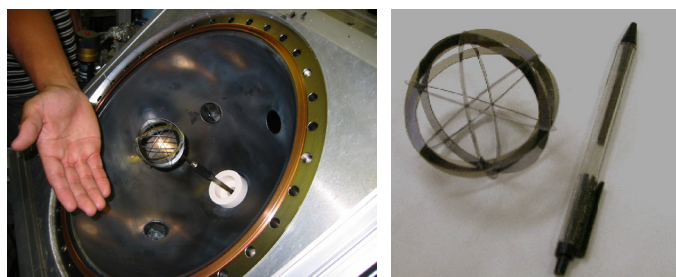


FIG. 2. An IECF device; a gridded cathode consisting of six ring-shaped Mo plates in a spherical chamber.

2. Experimental Setup

Our experimental device consists of a 340 mm diameter spherical vacuum chamber which serves as the anode and a highly transparent central gridded cathode of 60 mm diameter concentrically held by an insulator (Boron Nitride) as shown in Figs. 1 and 2. The highly transparent gridded cathode is made of six curved molybdenum sheets of 5 mm wide and 0.3 mm thick that are joined together by spot welding. Negative high voltages from a DC power supply are applied to the central cathode using a high voltage feedthrough.

As shown in Fig. 1, the IEC device is equipped to various control and diagnostic devices. The flow rates of D_2 and 3He gases are controlled by a mass flow controller and their respective partial pressures are measured by a capacitive manometer (MKS Baratron). A 3He proportional counter is equipped about 1 m apart from the cathode center for the neutron measurements.

A Li-implanted Si diode detector (Solid-State Detector: SSD) is placed at 330 mm apart from the center of cathode. The SSD has an effective detecting area of 600 mm² (27.6 mm diameter) and a 2 mm thickness capable of measuring the full energy of 14.7 MeV proton. For every incident proton, the SSD generates a single pulsed signal with an amplitude according to the proton energy, which is analyzed by a multi-channel analyzer (MCA) to provide the energy spectrum of the incident protons. The energy calibration of the SSD was done with α particles emitted from an ^{241}Am checking source. Difference of the SSD signal amplitude by an α particle from that by a proton is known to be small enough (less than 1 %) [7].

In the IEC device, the presence of energetic electrons and copious hard X-rays makes the proton measurement difficult. In addition, any detection system can suffer from deposition of the sputtered metallic ions. To mitigate this noise problem and the surface contamination of the detector, a metallic foil can be placed in front of the SSD to block metallic ions from sputtering, high energy electrons and hard X-rays. For example, a lead foil of 25 μm thickness was used in previous studies [3-6]. In order to evaluate the noise blocking efficiency of the foil, we investigated the stopping power of various metal foils. As shown in Fig. 3(a), although the thin lead foil is efficient to block the sputtered metallic ions, most of hard X-rays can penetrate the foil. Furthermore, the presence of the foil can lead to the reduction and energy-spread for the high energy protons to measure, resulting in the loss of signal fidelity especially for the D-D protons. In comparison, by use of a thinner foil, the energy spectrum of high energy protons is expected to be maintained as shown in Fig. 3(b), while on the other hand the X-ray transmission reaches $\sim 100\%$, higher than that by the thicker foils of $\sim 85\%$. In

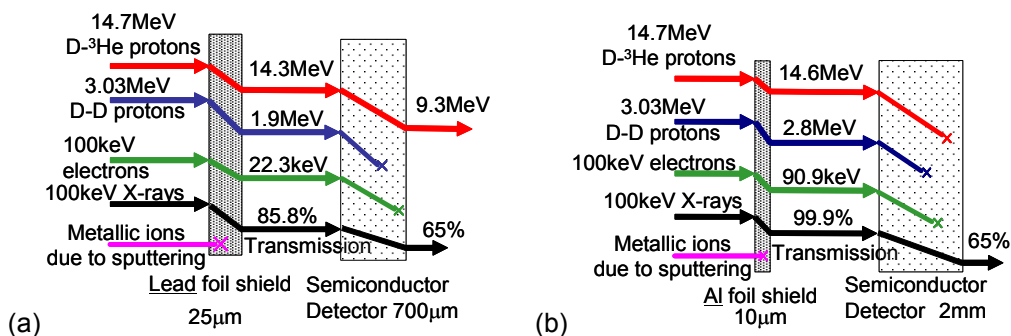


FIG. 3. Schematics of particle energy decays and X-ray transmittance through metallic foils in front of the SSDs; (a) a 25 μm thick lead foil in front of the SSD (700 μm) and (b) a 10 μm thick aluminum foil in front of the SSD (2 mm).

this study we compared two shielding foils, namely a 15 μm thick tungsten (almost equivalent to 25 μm thick lead) and a thinner foil of 10 μm thick aluminum experimentally. It is noted that for the both cases the high energy electrons of up to 100 keV to hit the detector surface can be blocked completely by use of a deflection magnet.

Between the IEC chamber and the SSD with the foil, circular collimator masks of three different diameters (25, 34 and 37 mm in diameter) were set on a linearly movable rod.

3. Experimental Results and Discussions

Figures 4 and 5 show typical signal spectra by the MCA. In Fig. 4, both the 14.7 MeV protons from $\text{D-}^3\text{He}$ fusions and 3.03 MeV protons from D-D fusions are clearly observed at slightly lower energies corresponding to the energy losses through the foils. At the same time the X-rays are seen to generate false signals in the low energy region. Although a single photon can generate a very low pulsed signal in the SSD compared with D-D protons of 3.03 MeV, the signals due to photons are found to be frequent enough to pile up and consequently overlap the D-D signals in the MCA spectrum.

We compared the two shielding foils, namely the 10 μm thick aluminum and 15 μm tungsten foils, in terms of this X-ray noise problem. As aforementioned, the former is almost transparent for X-rays. The latter in contrast can block X-rays to some extent ($\sim 85\%$

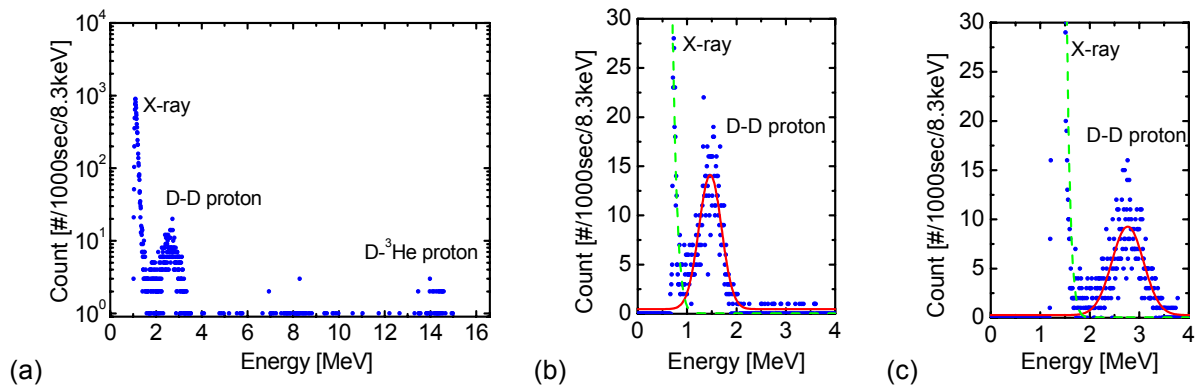


FIG. 4. Typical signal spectra by the SSD; (a) through the 10 μm thick aluminum foil, (b) magnified view for D-D proton energy range by use of the 10 μm thick aluminum foil and (c) the 15 μm thick tungsten foil.

$$(V_k = 40 \text{ kV}, I_k = 1.2 \text{ mA}, P_{3\text{He}}/P_{\text{Total}} = 0.75)$$

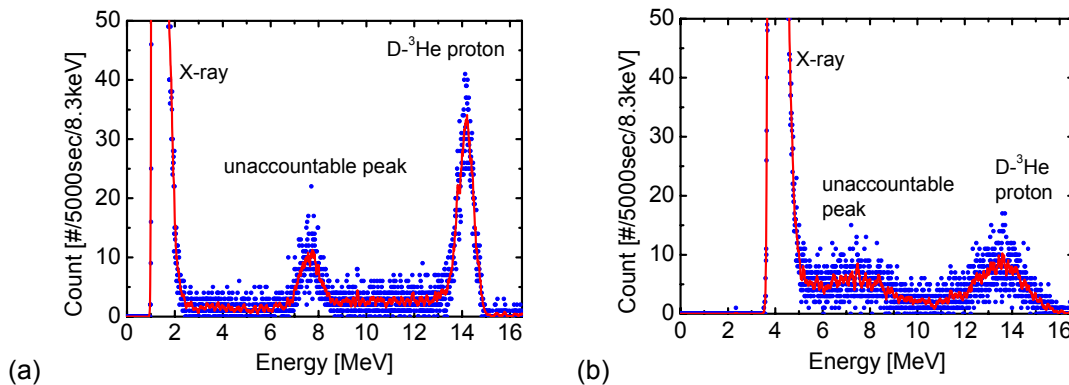


FIG. 5. SSD signal spectra for a higher power input, comparing the uses of (a) 10 μm aluminum and (b) 15 μm thick tungsten foils.

$$(V_k = 52 \text{ kV}, I_k = 2.5 \text{ mA}, P_{3\text{He}}/P_{\text{Total}} = 0.75)$$

transmission), while at the same time the protons to be counted tend to lose more energies through the tungsten foil than the aluminum. Experimental results shown in Fig. 4 agree these expectations, while the energy spread of the D-D signals is found unexpectedly larger by the use of the aluminum foil despite the energy spread induced by the thinner foil is expected to be smaller. As a result, the expected better separation of the D-D and X-ray signals by the use of the aluminum foil is found not to be significant.

As shown in Fig. 5, the noise from the X-rays greatly increases and appears in higher energy range when the discharge bias voltage and the current are increased up to $V_k = 52.0$ kV and $I_k = 2.5$ mA, respectively. As a result, we can no longer observe the D-D proton peak though a very clear D- 3 He peak can be obtained, because of the increased fusion reaction rate with increasing V_k and I_k . Again the D- 3 He proton peak is found to be much clearer by the use of the tungsten foil. The 15 μ m tungsten foil was then used hereafter.

It is to be noted that there is an unaccountable peak at ~ 8 MeV different from the signals of D-D or D- 3 He products, which will be discussed later.

3.1. Fusion Rate Dependences on D $_2$ - 3 He Composition

Figure 6(a) shows the neutron yield from D-D and the proton count rate from D- 3 He fusion reactions as functions of D $_2$ - 3 He gas composition. The fuel composition ratio in the figure, $P_{^3\text{He}}/P_{\text{Total}}$, is defined as the ratio of the partial pressure of ^3He gas to the total gas pressure of

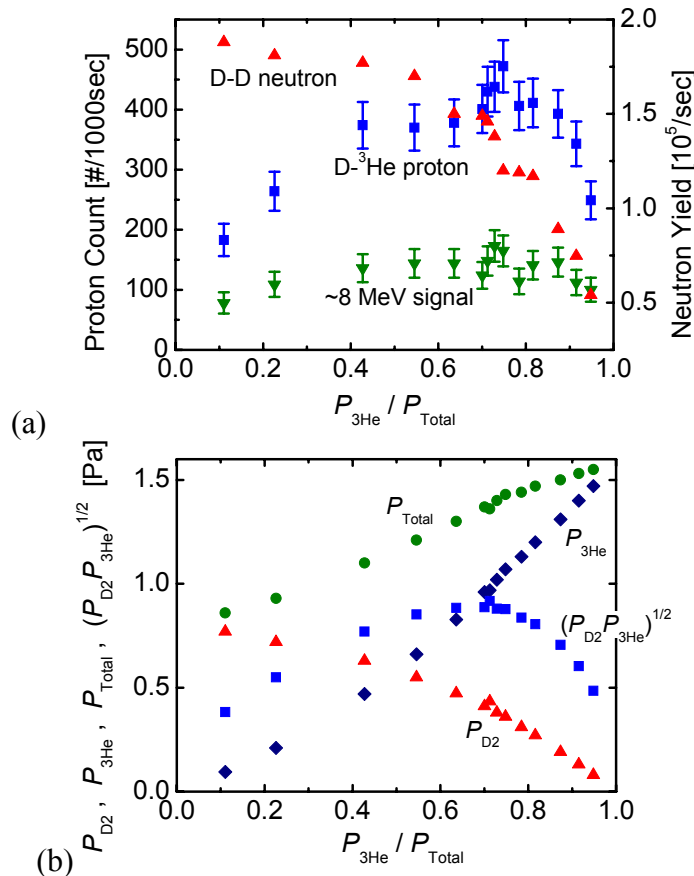


FIG. 6. (a) D-D neutron yield, D- 3 He proton count rate, and count rate of the unaccountable signals at ~ 8 MeV as functions of $P_{^3\text{He}}/P_{\text{Total}}$ and (b) dependences of the pressures for a constant $V_k = 52$ kV, and a constant $I_k = 2.5$ mA.

D_2 and 3He gases. The V_k and I_k were kept constant throughout as 52.0 kV and 1.2 mA, respectively. It is to be noted that P_{Total} increases with increasing $P_{^3He}/P_{Total}$, as shown in Fig. 6(b), because of the difference between the D_2 and 3He ionization cross-sections.

As shown in Fig. 6, the maximum $D-^3He$ proton production rate is obtained for $P_{^3He}/P_{Total}$ of ~ 0.7 , while in contrast the neutron yield from D-D fusion reactions decreases as $P_{^3He}/P_{Total}$ increases. Eventually, these tendencies are found to agree reasonably to $(P_{^3He} \cdot P_{D_2})^{1/2}$ and P_{D_2} as functions of $P_{^3He}/P_{Total}$, respectively, where P_{D_2} denotes the partial pressure of D_2 gas. Considering the constant I_k , this good agreement suggests the beam-gas fusion scenario rather than the beam-beam.

As of the unaccountable signals at ~ 8 MeV observed in Fig. 5, the dependence on $P_{^3He}/P_{Total}$ is seen well correlated to that of the $D-^3He$ proton counts, strongly implying the 14.7 MeV proton as the source.

3.2. Fusion Rate Dependences on Discharge Bias Voltage

Figure 7 shows the neutron yields from D-D fusion reactions and the proton counts from $D-^3He$ fusion reactions as functions of cathode bias voltage. A $P_{^3He}/P_{Total}$ of 0.75 is chosen for the optimized D_2-^3He proton production rate.

In Fig. 7, one can see that the $D-^3He$ fusion reaction rate increases more rapidly than the D-D fusion reaction rate with increasing discharge voltage. This can be explained by the difference of cross section dependences on the beam energy between D-D and $D-^3He$ reactions [8].

3.3. Spatial Distribution of $D-^3He$ Reaction

By use of the movable collimator masks, the count rates of both the $D-^3He$ proton signal and the unaccountable signal at ~ 8 MeV in Fig. 5 were measured as functions of the collimation geometry. Then, the Maximum Likelihood - Expectation Maximization (ML-EM) method [9], [10], which is commonly used in medical CT scanning, for example, for reconstructing a two-dimensional image from a set of projected one-dimensional images, was applied to reconstruct the spatial distribution of the proton yield shown in Fig. 8. In the reconstruction process, spherical symmetry was assumed except for the gridded cathode consisting of six ring-shaped molybdenum sheets (see the drawings in Fig. 8 and the photo in Fig. 2). The proton yield fractions on the six rings were treated as six independent variables.

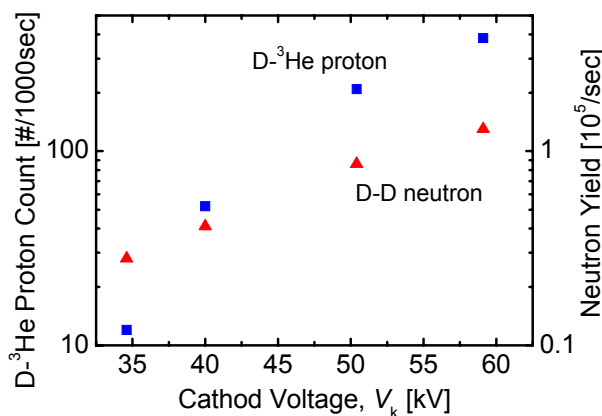


FIG. 7. D-D neutron yield and $D-^3He$ proton count rate as functions of discharge voltage. ($I_k = 2.5$ mA, $P_{^3He}/P_{Total} = 0.75$)

In Fig. 8(a), one can see both volumetric production of the $D\text{-}^3\text{He}$ protons and beam-target fusion, i.e. fusion between deuterium beam and ^3He embedded on the six rings. In contrast, in Fig. 8(b), the 8 MeV signal's birthplace is found localized strongly on one of the six rings which faces normal to the SSD observation direction. Eventually, the energy discrepancy is found to agree well with the energy loss of the 14.7 MeV proton through the 0.3 mm thick molybdenum sheet [11]. The reason for absence of the 8 MeV signal from the other rings is that the 14.7 MeV protons from the other rings would go through them with some angles to lose their whole energy.

Once the spatial profile is obtained, the total proton yield in the device can be calculated as well as the fractions of volumetric and embedded contributions. Their dependences on I_k for a fixed V_k of 60 kV and $P_{3\text{He}}/P_{\text{Total}}$ of 0.75 are shown in Fig. 9. The error bars in the figure result from statistical errors in the proton counting, i.e. we assumed an error of $\pm N^{1/2}$ for a proton count of N for every collimation geometry, and then all the errors are taken into account in the reconstruction process. The embedded fusion fraction is found to be $\sim 60\%$ almost regardless of I_k . As of the volumetric fusion contribution, the profile of proton yield density within the cathode is shown in Fig. 10(a) as a function of I_k . The error bars in the figure again correspond to the statistical errors in the proton counting. The fusion reaction density is found clearly to peak at the center. In Fig. 10(b) showing normalized density, the profile is seen to be broader for a higher I_k reasonably due to the space charge effect, though the broadening is not very significant under the present condition.

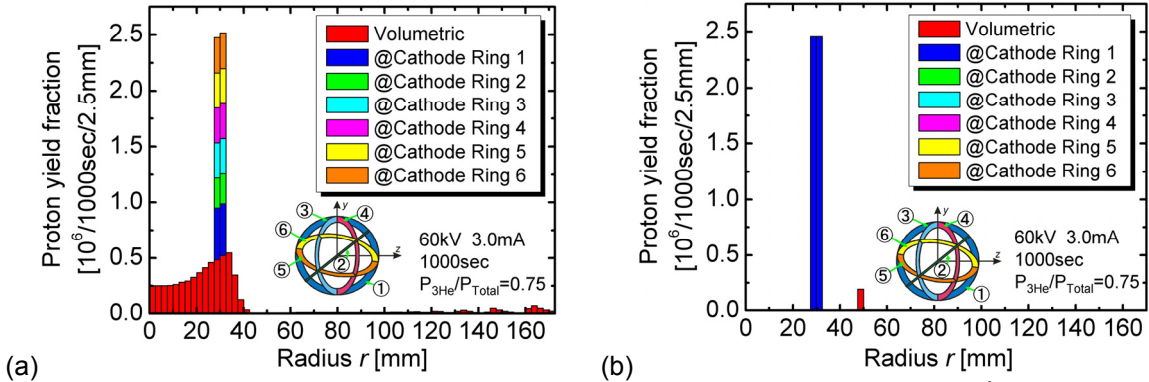


FIG. 8. Reconstructed spatial distributions of birthplaces of (a) the $D\text{-}^3\text{He}$ proton and (b) the unaccounted signals at ~ 8 MeV in Fig. 5.

$$(V_k = 60 \text{ kV}, I_k = 3.0 \text{ mA}, P_{3\text{He}}/P_{\text{Total}} = 0.75)$$

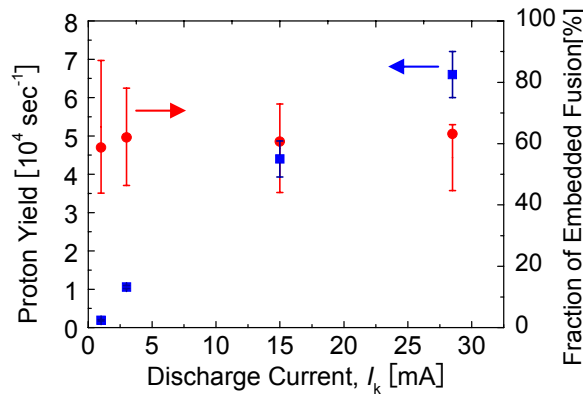
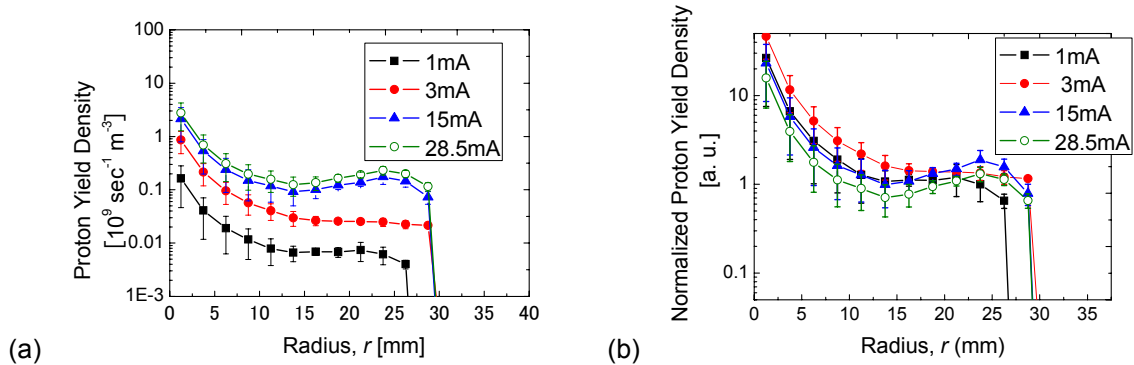


FIG. 9. Total $D\text{-}^3\text{He}$ proton yield and fraction of embedded fusion contribution as functions of discharge current. ($V_k = 60 \text{ kV}$, $P_{3\text{He}}/P_{\text{Total}} = 0.75$)



(a) (b)
 FIG. 10. Spatial profiles of volumetric fusion reaction density within the transparent cathode. Density profiles normalized by the total fusion rate are shown in (b).

4. Conclusions

High energy protons from D-³He (14.7 MeV) fusion reactions have been successfully measured using a proton counting system employing a shielding foil, a deflecting magnet and a 2 mm thick SSD, though the hard X-ray remains a big source of noise, which requires further improvement in the detector system for detecting D-D protons (3.03 MeV). The reaction rates have been measured as functions of D₂ and ³He fuel composition. The maximum D-³He proton production rate is obtained for the fuel composition ratio, $P_{3\text{He}}/P_{\text{Total}}$, of ~ 0.7 , i.e. ³He rich gas mixture. The dependences of D-D and D-³He reaction rates on the fuel composition show good agreements with those of the partial pressure of D₂, P_{D_2} , and $(P_{3\text{He}} \cdot P_{\text{D}_2})^{1/2}$, respectively, strongly implying beam-gas and/or beam-target fusion scenario rather than beam-beam collisions. In addition, the fusion reaction rates have been measured as functions of the discharge voltage, which agree with the functional tendencies of D-D and D-³He fusion cross sections. The present proton counting system and analysis scheme have successfully revealed the spatial distribution of D-³He proton yield. The volumetric fusion contribution is found $\sim 40\%$, which is encouraging compared with the imprecation of predominant embedded fusion contribution by previous studies. Also, the volumetric fusion is seen to peak at the center and well concentrated within the transparent cathode.

References

- [1] B. B. Cipiti et al., Fusion Sci. and Tech. **44** (2003) 534-538.
- [2] J. W. Weidner et al., Fusion Sci. and Tech. **44** (2003) 539-543.
- [3] R. P. Ashley et al., "Fusion Product Source Region in the IEC Fusion Reactor", 5th US-Japan Workshop on IEC Fusion, Madison, WI, October 9-10, 2002, <http://fti.neep.wisc.edu/iecworkshop/agenda.html>.
- [4] R. P. Ashley et al., Fusion Technology **39** (2001) 546-551.
- [5] R. P. Ashley et al., Fusion Sci. and Tech. **44** (2003) 564-566.
- [6] K. Masuda et al., Fusion Technology **39** (2001) 562-566.
- [7] I. Kimura et al., Radioactive Rays Measurements Handbook, chapter 11, Nikkankogyo Shimbun LTD, 1991, in Japanese.
- [8] (a) Nuclear cross section data, G.H. Miley, H. Towner and N. Ivich, *Fusion Cross Section and Reactivities*, Rept. COO-2218-17, University of Illinois, Urbana, IL, 1974.
 (b) B.H. Duane, *Fusion Cross Section Theory*, Rept. BNWL-1685, Brookhaven National Laboratory, 1972.
- [9] T. K. Moon, IEEE Signal Processing Magazine (1996) 47-60.
- [10] H. Zen et al., Proc. of 27th International Free Electron Laser Conf. (2005) 592-595.
- [11] J.F. Ziegler, *the Stopping Ranges of Ions in Matter*, vol. 4, Pergamon Press (1977).